



# Management on the location and concentration of $\text{Ti}^{3+}$ in anatase $\text{TiO}_2$ for defects-induced visible-light photocatalysis

Xiaoye Xin<sup>a,b</sup>, Tao Xu<sup>c</sup>, Jiao Yin<sup>a</sup>, Lan Wang<sup>a,\*</sup>, Chuanyi Wang<sup>a,\*</sup>

<sup>a</sup> Laboratory of Environmental Sciences and Technology, Xinjiang Technical Institute of Physics & Chemistry; Key Laboratory of Functional Materials and Devices for Special Environments, Chinese Academy of Sciences, Urumqi 830011, PR China

<sup>b</sup> University of Chinese Academy of Sciences, Beijing 100049, PR China

<sup>c</sup> Department of Chemistry and Biochemistry, Northern Illinois University, DeKalb, IL 60115, USA

## ARTICLE INFO

### Article history:

Received 7 February 2015

Received in revised form 7 April 2015

Accepted 8 April 2015

Available online 9 April 2015

### Keywords:

Anatase  $\text{TiO}_2$  nanocrystal

$\text{Ti}^{3+}$

Defects-induced

Photocatalysis

Visible light

## ABSTRACT

The defect-induced “black-and-white” issue of  $\text{TiO}_2$  keeps this material under spotlight in the past decade. This work exhibits an oxidation-based synthesis of anatase  $\text{TiO}_2$  nanocrystals with various  $\text{Ti}^{3+}$  concentrations via a solvothermal process in combination with post-annealing at different temperatures. Strikingly, we found that by simply controlling the annealing temperature, both concentration and location of the  $\text{Ti}^{3+}$  defects can be well managed to reside predominately in the subsurface/bulk regions of the post-annealed anatase  $\text{TiO}_2$  nanocrystals, a highly desired feature for stable visible light-active photocatalysis. The location and quantity of the  $\text{Ti}^{3+}$  in anatase nanocrystals pinpointed by X-ray photoelectron spectroscopy (XPS) and electron paramagnetic resonance (EPR) suggest that this temperature-mediated management of the location and concentration of  $\text{Ti}^{3+}$  defects is achieved through a  $\text{Ti}^{3+}$  reversible-diffusion mechanism. As an applicable verification, the sample attained by post-annealing treatment at 500 °C, which has the highest  $\text{Ti}^{3+}$  concentration predominately in the bulk region, exhibits a 30-fold enhancement in visible-light decomposition of methylene blue and 4 times improvement in the maximal transient photocurrent density compared with P25. This work reveals that managing the location and concentration of  $\text{Ti}^{3+}$  defects in  $\text{TiO}_2$  is a decisive process toward defects-induced visible-light photocatalysis.

© 2015 Elsevier B.V. All rights reserved.

## 1. Introduction

Titanium dioxide ( $\text{TiO}_2$ ) has been a topic of extensively studied metal oxide materials in the last decades, especially in the arena of energy and environmental applications [1–4]. However, its wide band gap (~3.2 eV) makes it capture only about 5% of solar energy, which greatly hinders its light harvesting efficiency [5,6]. Many efforts have been directed to enhance the light harvesting of  $\text{TiO}_2$  in visible region (accounts for ~43% of the solar energy) through doping of impurity atoms to narrow the band gap [7–11]. Nevertheless, such band structure engineering may induce issues such as carrier trapping, thermal/crystal instability, secondary contamination by dopants etc.

Defects in materials often exhibit unusual effects that could lead to significant advancement in various scientific fields [12,13]. Well-managed defects (e.g., impurity, structural vacancies etc.) in terms of their location and concentration in materials can result in more desired properties. Recently, the chemistry of structurally defective  $\text{TiO}_2$  with  $\text{Ti}^{3+}$  self-doping (or oxygen vacancies) has been developed to tackle the above challenges [14–17]. In general,  $\text{Ti}^{3+}$  self-doping is induced by reducing solid  $\text{TiO}_2$  particles with a suitable reductant in gas or solution phase. Hence, the reduction is always initiated on the surface of the solid  $\text{TiO}_2$  nanoparticles. Consequently,  $\text{Ti}^{3+}$  defects are generated predominantly on the surface of  $\text{TiO}_2$  and can be easily oxidized by air or the dissolving oxygen in water [3,18]. Alternatively, reduction can also be achieved by harsh and costly physical methods, such as high temperature and pressurized hydrogenation [19–22], plasma treatment [23,24], vacuum activation and electron beams irradiation [25]. Considering all these disadvantages associated with the reduction-based synthesis of  $\text{Ti}^{3+}$ -self doped  $\text{TiO}_2$ , the counter-intuitive strategy, that is, oxidation of precursory materials in which titanium is in

\* Corresponding authors. Tel.: +86 991 3835879; fax: +86 991 3838957.

E-mail addresses: [wanglan@ms.xjb.ac.cn](mailto:wanglan@ms.xjb.ac.cn) (L. Wang), [cyywang@ms.xjb.ac.cn](mailto:cyywang@ms.xjb.ac.cn) (C. Wang).

its lower oxidation state than Ti(IV), becomes an intelligent choice. The starting materials such as  $\text{TiH}_2$ ,  $\text{TiO}$ ,  $\text{Ti}_2\text{O}_3$  or even Ti can be oxidized under a mild reaction condition to yield  $\text{Ti}^{3+}$ -doped  $\text{TiO}_2$  [18,26,27]. Furthermore, the  $\text{Ti}^{3+}$  defects in  $\text{TiO}_2$  have also been theoretically studied, and the results suggest that the concentration of  $\text{Ti}^{3+}$  plays a decisive role in producing a facile transfer of an electron or hole [28,29] to gain an efficient activity in the visible spectrum. Grabstanowicz et al. [29] developed an inorganic chemistry-based method to induce high-concentration  $\text{Ti}^{3+}$  in the bulk, which exhibits visible-light photocatalytic activity. Yu et al. [30] optimized the hydrogenation temperature and time, and found that high surface-to-bulk ratio of defects significantly enhances the photoactivity. However, the impact of distribution of bulk and/or surface defects on the activity of  $\text{TiO}_2$ -based photocatalysts still remains unclear.

To unveil the role of  $\text{Ti}^{3+}$  defects in photocatalysis, a facile and efficient method is highly desirable to manage the distribution and concentration of  $\text{Ti}^{3+}$ , and consequently, understand their impact on the defects-induced visible-light photoactivity. In this work, we have developed an innovative facial oxidation-based solvothermal method to synthesize bulk  $\text{Ti}^{3+}$  self-doped anatase  $\text{TiO}_2$  nanocrystals ( $\text{TiO}_{2-x}$ ). The distribution of subsurface/bulk defects can be controlled by further annealing the as-prepared  $\text{TiO}_{2-x}$  at different temperatures. Based on experimental observations, we first propose a “ $\text{Ti}^{3+}$  reversible-diffusion mechanism”, demonstrating that “ $\text{Ti}^{3+}$ ”-induced photoactivity relies on not only the absolute defect concentration, but also on a proper distribution of the subsurface/bulk defects.

## 2. Experimental

### 2.1. Materials

Titanium hydride ( $\text{TiH}_2$ , 98.0%) powder was purchased from Sigma-Aldrich Co., LLC. Hydrogen peroxide ( $\text{H}_2\text{O}_2$ , 30.0%), sodium borohydride ( $\text{NaBH}_4$ , 98.0%), absolute ethyl alcohol ( $\text{EtOH}$ , 99.9%), hydrochloric acid ( $\text{HCl}$ , 36–38%, A.R.) and sodium hydroxide ( $\text{NaOH}$ , 98%, A.R.) were obtained from Sinopharm Chemical Reagent Co., Ltd. and used as received without any further purification. Double distilled water was used throughout the experiments.

### 2.2. Synthesis of $\text{Ti}^{3+}$ self-doped anatase $\text{TiO}_2$ nanoparticles

In a typical synthetic process,  $\text{TiH}_2$  (0.256 g) and  $\text{H}_2\text{O}$  (2 mL) were mixed in a 50 mL round-bottomed flask magnetically stirred for 5 min. Then  $\text{H}_2\text{O}_2$  (30 mL 30.0 wt%) was added dropwise to this dark gray suspensions, and this mixture was vigorously stirred for 12 h till it changed to yellowish gel-like state. After that,  $\text{EtOH}$  (40 mL) was added under continuous magnetic stirring. A certain amount of  $\text{NaOH}$  (1.0 M) solution was added gradually until the pH of the mixture solution was tuned to 9.0.  $\text{NaBH}_4$  (0.4 g) as an antioxidant was added to this light yellow transparency mixture and then transferred to the Teflon-lined stainless-steel autoclave (capacity: 100 mL) immediately and solvothermally treated at 180 °C for 24 h. The sample was then collected and added into  $\text{HCl}$  (50.0 mL, 1.0 M) solution to eliminate the sodium boron compounds. After stirring for 10 h, the powders were washed by distilled water and ethanol repetitively to remove the impurities (e.g.,  $\text{Na}^+$ ,  $\text{Cl}^-$ ,  $\text{BO}_3^{2-}$ ). The obtained precipitate was dried under vacuum for 12 h to yield a light blue  $\text{TiO}_2$  nanocrystals powder, denoted as  $\text{TiO}_{2-x}$ . Post-annealing treatment of the  $\text{TiO}_{2-x}$  sample was conducted under a  $\text{N}_2$  gas flow (150 sccm) in a tube furnace at an elevated temperature in the range of 300–700 °C for 3 h and heating rate was set as 4 °C/min. Therefore, the samples obtained at different temperatures are designated as  $\text{TiO}_{2-x-T}$ , where  $T$  refers to the post-annealing temperatures (°C).

### 2.3. Structural characterization

The crystal structures of the samples were identified on a Bruker D8 X-ray diffractometer with Cu K $\alpha$  radiation ( $\lambda = 0.15418 \text{ nm}$ ). The morphology photographs of the samples were recorded by field emission scanning electron microscopy (FESEM; ZEISS SUPRA55VP) and transmission electron microscopy (TEM, JEOL-JEM 2100). Brunauer–Emmett–Teller (BET) surface area of the samples was measured by  $\text{N}_2$  adsorption/desorption isotherms recorded at 77 K (QUADRASORB IQ, Quantachrome Instrument Corp.). Before the measurements, samples were degassed at 150 °C overnight. Ultraviolet-visible (UV-vis) diffusion reflectance spectra of the samples were obtained on a SolidSpec-3700DUV spectrophotometer (Shimadzu) using  $\text{BaSO}_4$  as reference to obtain absorption spectra for determining the band gap. Raman spectra were obtained on a laser Raman spectrometer (LabRAM HR Evolution RAMAN SPECTROMETER, HORIBA Scientific Ltd.) with a back scattering configuration using an Ar $^+$  laser (20 mW, 532 nm) as excitation source. The surface electronic state analysis was studied by X-ray photoelectron spectra (XPS), and the measurements were carried out on an X-ray photoelectron spectrometer (ESCALAB MK II) using Mg K $\alpha$  (1253.6 eV) X-rays as the excitation source, with C 1s (284.6 eV) for calibration. Thermo gravimetric analysis (TGA) was performed on a NETZSCH STA 449F3 instrument, model Pyris 1 system under an air flow of 50 mL/min and the measurement was conducted under air flow at a heating rate of 10 °C/min. Electron paramagnetic resonance (EPR) spectra were recorded on a Bruker Elexsys E500 spectrometer by applying an X-band (9.43 GHz, 1.5 mW) microwave with sweeping magnetic field at 110 K in cells that can be connected to a conventional high-vacuum apparatus (residual pressure  $< 10^{-4}$  mbar). The concentration of  $\text{Ti}^{3+}$  was determined by a numerical double integration of the EPR spectra in comparison with an aqueous solution of  $\text{Cu}^{2+}$ . The photocurrent responses and electrochemical impedance spectra (EIS) were performed on an electrochemical station (CHI660E, Chenhua, China).

### 2.4. Measurement of photocatalytic activity.

The visible light photocatalytic activity of the  $\text{Ti}^{3+}$  self-doped anatase  $\text{TiO}_2$  nanoparticle was assessed by the degradation of methylene blue (MB) dye, a common dye contaminant presented in the waste water from textile industry. In a typical experiment, a 300 W Xe lamp (PLS-SXE300, Perfect Light Company, Beijing, China) equipped with an ultraviolet cut-off filter was employed as the light source to provide visible light ( $\geq 420 \text{ nm}$ ). The illumination intensity at the surface was  $0.216 \text{ W/cm}^2$  as measured by a calibrated precision optical power meter (1916-C, Newport Corp.). The degradation experiment was carried out in a 150 mL reactor accommodated with a circulating water cooling system. In order to attain an optimally dispersed system and reach entirely adsorption–desorption equilibration, 20 mg of photocatalyst was dispersed into MB (100 mL, 20 mg/L) solution after supersonic treatment for 5 min, then the mixture was stirred in dark for 40 min and the pH value of the reaction system was 7.0. The suspension (3.4 mL) was withdrawn periodically from the reactor at certain interval, then the photocatalyst was separated by centrifugation and the concentration of residual MB solution was monitored by UV-vis spectrophotometer (UV-2550, Shimadzu, Japan) during the whole experiment.

### 2.5. Measurement of photocurrent.

Five milligrams of photocatalysts were dispersed in nafion (0.5 wt%) solution and ultrasonically vibrated for 10 min. The resultant slurry (0.25 mL) was then dip-coated onto a  $10 \times 10 \text{ mm}$  indium-tin oxide (ITO) glass electrode and dried under room

temperature overnight to eliminate ethanol. The prepared  $\text{TiO}_{2-x}/\text{ITO}$  electrode, platinum electrode, and saturated potassium chloride electrode (SPCE) were used as the working electrode, counter electrode, and reference electrode, respectively. The electrolyte was  $\text{Na}_2\text{SO}_4$  (20 mL 0.1 mol/L) aqueous solution. The working electrode was activated in the electrolyte for 0.5 h prior to measurement. A 300W Xe lamp, which generates light with its maximum intensity at 420 nm, was used as light source. The intensity of photocurrent was measured by an electrochemical workstation (CHI660C, Chenhua, China).

## 2.6. Products analysis.

The products formed from the MB decomposition was analyzed using the high performance liquid chromatography (Agilent 1290)/mass spectrometry (HPLC-MS) system equipped with a Water BEA C<sub>18</sub> column (2.1 mm × 100 mm, 1.9 μm). The eluent, consisting of methanol (A) and ultrapure water (B), served as the mobile phase in a gradient mode (20% A, 80% B) at a flow rate of 0.2 mL/min. Mass analysis was performed with the Q1 full-scan negative ion mode electrospray ionization (ESI) mass of a TSQ QUANTUM ULTRA (thermo), mass spectrometer. The reaction samples taking at different time intervals during the reaction were analyzed by introducing the aliquots into the ESI source. Typical ESI measurements were conducted under conditions of heated capillary temperature at 300 °C, sheath gas N<sub>2</sub> at a flow rate of 30 units, cone voltage of 30 V, and capillary voltage of 3.5 eV. The total organic carbon (TOC) tests for samples at different time intervals were conducted on a vario TOC (Elementar, Germany) analyzer. This instrument was calibrated with standard solution of potassium hydrogen phthalate.

## 3. Results and discussion

### 3.1. Characterization of $\text{Ti}^{3+}$ self-doped anatase $\text{TiO}_2$

**Fig. 1a** evidently shows that all samples are presented in various coloration which are remarkably different from white perfect  $\text{TiO}_2$  nanocrystal particles, indicating the existence of  $\text{Ti}^{3+}$  [31]. The initial light blue  $\text{TiO}_{2-x}$  nanoparticles obtained after hydrothermal synthesis change their color dramatically when treated via a controllable post-annealing process. At the first stage of post-annealing treatment process (300 °C), the color of the sample changes from light blue to light brown. With increasing the temperature, the color of the as-prepared  $\text{TiO}_{2-x}$  powder deepens to brown (400 °C) and finally becomes an intense dark black color at 500 °C. As the post-annealing treatment temperature further increases, the dark black color is not maintained but readily changed to a dark brown at 600 °C and gradually faded to a slightly shallow dark brown at 700 °C. More importantly, the color of individual  $\text{Ti}^{3+}$  self-doped  $\text{TiO}_2$  samples maintain unchanged for 8 months at ambient condition, suggesting the great stability of the defects.

X-ray diffraction (XRD) analysis was conducted to identify the crystal structures and crystallite size of the samples. As indicated by XRD patterns (**Fig. 1b**), all as-received  $\text{TiO}_2$  samples have a typical anatase structure without any impurity phase in agreement with the JCPDS card No. 21-1272. By increasing the post-annealing temperature, the defective  $\text{TiO}_2$  diffraction peak becomes stronger and sharper due to the increase of crystallinity. When the temperature reaches 700 °C, the maximum peak intensity is observed. It is worth noting that treatment at the highest temperature does not induce crystal phase transition, suggesting that the present controlled synthesis of  $\text{TiO}_2$  nanocrystals with different subsurface/bulk  $\text{Ti}^{3+}$  distributions can suppress phase transformation from anatase to rutile. The crystallite size of  $\text{TiO}_{2-x}$ ,  $\text{TiO}_{2-x}-300$ ,

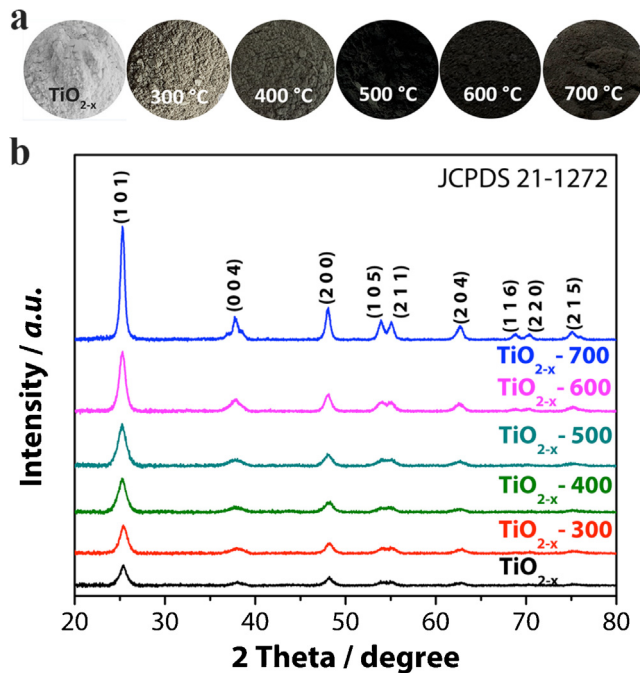


**Fig. 1.** (a) Photographic images of  $\text{Ti}^{3+}$  self-doped  $\text{TiO}_2$  samples prepared with post-annealing treatment in the range of 300–700 °C for 3 h in a  $\text{N}_2$  gas flow. (b) XRD patterns of as-prepared  $\text{TiO}_{2-x}$  and  $\text{TiO}_{2-x}-T$  samples. (For interpretation of the references to color in the text, the reader is referred to the web version of this article.)

**Table 1**  
Physico-chemical properties of  $\text{TiO}_{2-x}$  samples.

Sample	Crystallite size (nm)		$S_{\text{BET}}$ (m <sup>2</sup> g <sup>-1</sup> )	Optical band gap (eV) <sup>c</sup>
	XRD <sup>a</sup>	TEM <sup>b</sup>		
$\text{TiO}_{2-x}$	8.9	14.3	272.87	3.12
$\text{TiO}_{2-x}-300$	9.1	14.5	245.96	3.03
$\text{TiO}_{2-x}-400$	9.2	14.5	235.06	2.85
$\text{TiO}_{2-x}-500$	9.5	14.8	170.48	2.63
$\text{TiO}_{2-x}-600$	9.7	14.8	147.80	2.67
$\text{TiO}_{2-x}-700$	14.2	14.9	78.98	2.75

<sup>a</sup> Estimated by the Scherrer equation from the broadening of anatase (101) reflection in XRD, respectively.

<sup>b</sup> Estimated by TEM observation.

<sup>c</sup> Estimated by Kubelka-Munk function.

$\text{TiO}_{2-x}-400$ ,  $\text{TiO}_{2-x}-500$ ,  $\text{TiO}_{2-x}-600$  and  $\text{TiO}_{2-x}-700$  determined by using Sherrer's formula ( $L=0.89\lambda/\beta\cos\theta$ ) is 8.9, 9.1, 9.2, 9.5, 9.7 and 14.2 nm, respectively. These results agree well with our BET results, which is 272.87, 245.96, 235.06, 170.48, 147.80 and 78.98 cm<sup>2</sup>/g for sample  $\text{TiO}_{2-x}$ ,  $\text{TiO}_{2-x}-300$ ,  $\text{TiO}_{2-x}-400$ ,  $\text{TiO}_{2-x}-500$ ,  $\text{TiO}_{2-x}-600$  and  $\text{TiO}_{2-x}-700$ , respectively (**Table 1**). Apparently, the high temperature post-annealing treatment induces the growth of crystalline but decreases the surface area.

UV-vis diffuse reflectance spectra (DRS) were recorded to study the optical properties of the  $\text{Ti}^{3+}$  self-doped anatase  $\text{TiO}_2$  nanoparticles. As shown in **Fig. 2a**, the as-prepared  $\text{TiO}_{2-x}$  sample (light blue in color) exhibits a slight lower absorbance under UV region, however, a stronger absorption between 400 and 800 nm compared to P25. This strong absorption is attributed to the existence of bulk  $\text{Ti}^{3+}$  defects which induce a continuous vacancy band of electronic states just below the conduction band edge of  $\text{TiO}_{2-x}$ . In comparison with  $\text{TiO}_{2-x}$ , the photon absorption of  $\text{TiO}_{2-x}-T$  significantly extends into longer wavelengths, maintaining a high level of absorption covering the entire visible light region. The stronger absorption in the visible-light region helps the utilization of solar light, giving rise to more photogenerated electrons and holes for

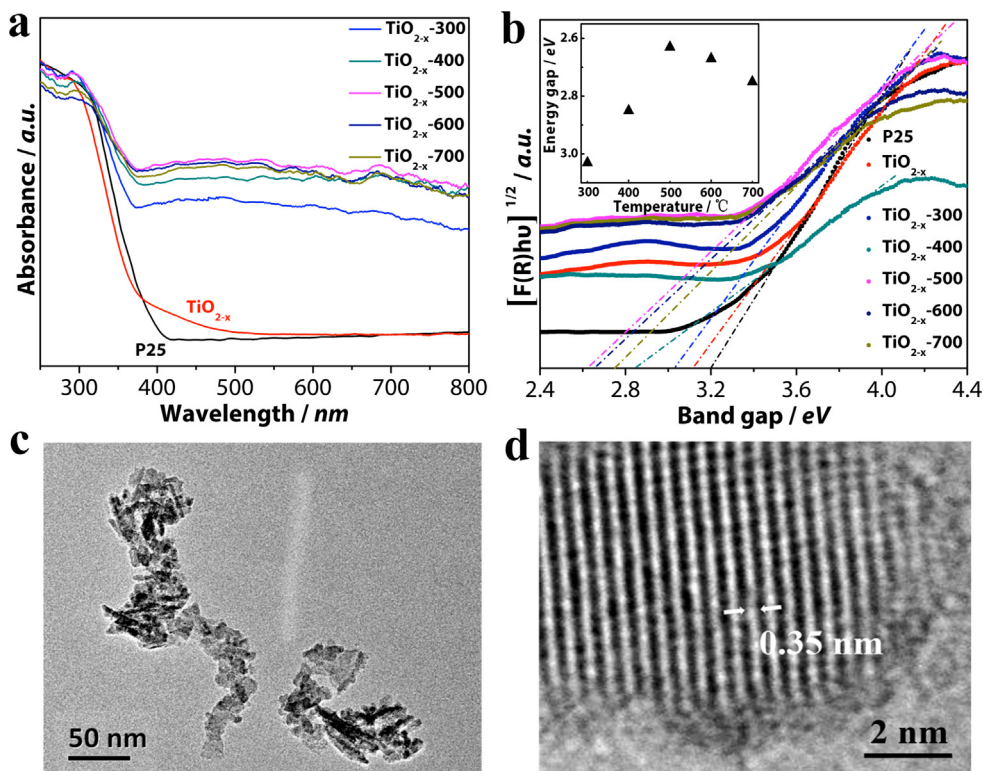


**Fig. 2.** (a) UV-vis diffuse reflectance spectra of the as-prepared anatase  $\text{TiO}_{2-x}$  and  $\text{TiO}_{2-x}\text{-}T$  nanoparticles in comparison to pure P25. (b) Curves of Kubelka–Munk function as the vertical axis and plotted it against the photon energy. The top left insert is optical band gap of  $\text{TiO}_{2-x}\text{-}T$  samples. (c) TEM and (d) HRTEM images of a typical  $\text{TiO}_{2-x}\text{-}500$  sample. (For interpretation of the references to color in the text, the reader is referred to the web version of this article.)

subsequent photocatalytic reactions. Interestingly, the absorption threshold changes in the case of post-annealing at different temperatures. All  $\text{TiO}_{2-x}\text{-}T$  samples show a larger redshift of the absorption edge with respect to the  $\text{TiO}_{2-x}$  sample. Furthermore, a monotonic increase of redshift shows up in the UV–vis DRS spectra of  $\text{TiO}_{2-x}\text{-}T$  ( $T$  is 300, 400 and 500) samples, while a slight blue shift appears at  $\text{TiO}_{2-x}\text{-}600$  and a further inconspicuous blue shift happens on  $\text{TiO}_{2-x}\text{-}700$ . Meanwhile, the absorption edge of  $\text{TiO}_{2-x}\text{-}600$  and  $\text{TiO}_{2-x}\text{-}700$  are on the right side of the  $\text{TiO}_{2-x}\text{-}400$ , which is coincident with the observed color change trend of  $\text{TiO}_{2-x}\text{-}T$  samples (as depicted in Fig. 1a). Using the Kubelka–Munk function as the vertical axis to plot it against the photon energy, as shown in Fig. 2b, the optical band gaps of all samples can be derived, and the results are summarized in Table 1. Among all the samples, the band gap of  $\text{TiO}_{2-x}\text{-}500$  (2.63 eV) is the narrowest one due to the most abundant well-dispersed  $\text{Ti}^{3+}$  defects in the bulk phase of the  $\text{TiO}_2$  lattice, as evidenced by EPR study discussed in the later section.

The phase structures of  $\text{Ti}^{3+}$  self-doped  $\text{TiO}_2$  nanoparticles were investigated by transmission electron microscopy (TEM). The TEM images of a typical  $\text{Ti}^{3+}$  self-doped  $\text{TiO}_2$  sample prepared with post-annealing treatment at 500 °C ( $\text{TiO}_{2-x}\text{-}500$ ) is presented in Fig. 2. The average particle size is ca. 14.8 nm with a truncated octahedron bipyramids morphology, each of which is a single anatase crystal without obvious aggregation (Fig. 2c). Unlike the nanoparticles produced by vacuum calcination or hydrogenation methods [23–25,28], the obtained  $\text{Ti}^{3+}$  self-doped  $\text{TiO}_{2-x}$  samples are uniformly dispersed. The uniform lattices indicate that the  $\text{Ti}^{3+}$  self-doped  $\text{TiO}_2$  nanoparticles are highly crystallized. All the samples with post-annealing treatment at different temperatures ( $\text{TiO}_{2-x}\text{-}T$ ) show the lattice spacing of  $d = 0.352 \text{ nm}$ , inconsistency with theoretical value of anatase phase (1 0 1) facet (Fig. 2d). There is no obvious difference in lattice fringes width (e.g., those for

rutile phase or  $\text{TiH}_2$ ), indicating that the as-prepared sample is pure anatase phase.

To further examine the structure characteristics and crystal deficiency of  $\text{Ti}^{3+}$  self-doped  $\text{TiO}_2$  nanoparticles, Raman spectral measurements were conducted (Fig. 3a). Degussa P25 was employed in the same phase composition analysis as reference. The six characteristic Raman active modes ( $3E_g + 2B_{1g} + A_{1g}$ ) with frequencies at 144, 197, 397, 513, 519 (superimposed with the 513 cm<sup>-1</sup> band) and 639 cm<sup>-1</sup> observed in all samples are indexed as the tetragonal structure of anatase phase with  $D_{4h}$  space group ( $I_{41}/\text{amd}$ ) [32]. This confirms the formation of well-crystallized anatase  $\text{TiO}_2$  nanoparticles in the solvothermal synthesis.

More importantly, there are no Raman peaks of rutile or brookite phase  $\text{TiO}_2$ , demonstrating the crystal phase of all samples is of pure anatase  $\text{TiO}_2$ , after post-annealing treatment, in agreement with the XRD results. Generally, Raman modes derived from different crystal facets make different contribution to the Raman-active modes. For this reason, Raman spectroscopy has long been used to analyze the percentage of specific exposed facets in anatase  $\text{TiO}_2$  [33]. As shown in Fig. 3a, the different Raman vibrational modes almost maintain the same peak ratio, suggesting that the percentage of specific exposed facets remains unchanged during the post-annealing treatment process. However, the most remarkable feature is that the predominated peak position undergoes a blue shift from 144.4 cm<sup>-1</sup> to 152.6 cm<sup>-1</sup> accompanied by peak broadening for  $\text{TiO}_{2-x}$  and  $\text{TiO}_{2-x}\text{-}T$  samples compared to P25 (see inset of Fig. 3a). As reported previously, the  $E_g$  mode shift and broadened linewidth of  $\text{TiO}_2$  in Raman spectrum can be ascribed to a lattice disorder or localized defects associated with oxygen vacancies [34,35]. Thus, the blue shift of  $E_g$  mode for 8.2 cm<sup>-1</sup> found in  $\text{TiO}_{2-x}\text{-}T$  samples and the broadening of the peaks support the presence of lattice disorder (nonstoichiometric) and crystal domain size effect [36]. Furthermore, it is observed that the intensity of Raman

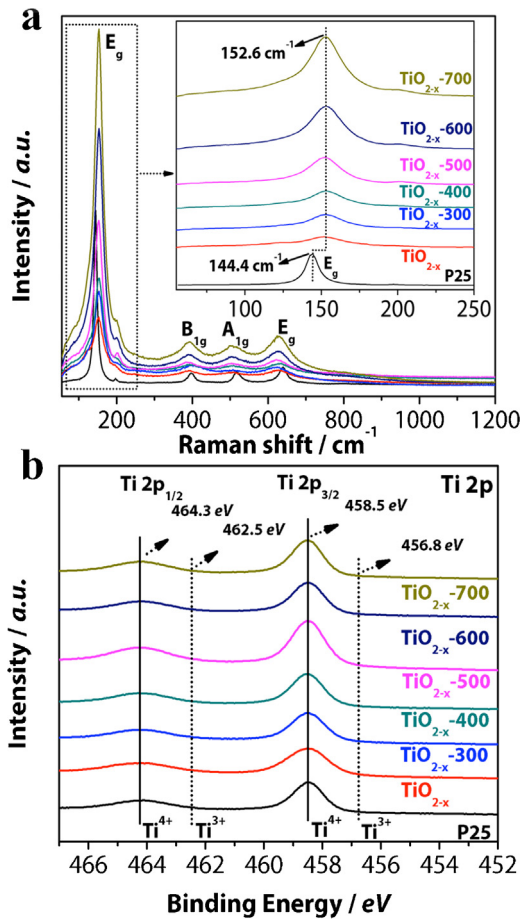


**Fig. 3.** (a) Raman spectra of Degussa P25,  $\text{TiO}_{2-x}$  and  $\text{TiO}_{2-x}-T$  samples. The inset is the high-resolution  $E_g$  mode of the samples. (b) XPS patterns of Degussa P25, as-prepared  $\text{TiO}_{2-x}$  and  $\text{TiO}_{2-x}-T$  samples. (For interpretation of the references to color in the text, the reader is referred to the web version of this article.)

vibration modes increases as the post-annealing treatment temperature increases. We attributed this effect to the enhanced crystallinity upon the increase in annealing temperature, because bigger crystallinity contains more Raman active facets, which is proportional to the  $E_g$  intensity fluctuations.

### 3.2. The location and concentration of $\text{Ti}^{3+}$ in anatase $\text{TiO}_2$

To probe the presence and chemical states of Ti in surface region of the as-prepared  $\text{TiO}_{2-x}-T$  samples, XPS measurement was carried out because XPS is only surface sensitive up to ca. 5 nm beneath the top surface layer. As shown in Fig. 3b, for all samples, the  $\text{Ti} 2p_{3/2}$  peak maximum is centered at 458.5 eV and the peak is highly symmetric, indicating absolute coordination of  $\text{Ti}^{4+}$  [37]. The peak at 464.3 eV is assigned to the  $2p_{1/2}$  core level of  $\text{Ti}^{4+}$  in  $\text{TiO}_2$ . Surprisingly, the Ti core level XPS spectra of as-prepared  $\text{TiO}_{2-x}$  and the post-annealing  $\text{TiO}_{2-x}-T$  samples are almost unanimously comparable to that of Degussa P25 as reported previously in  $\text{TiO}_{2-x}$  [38], suggesting the existence of identical surface state of Ti in these samples.

XPS clearly suggests that there is no detectable Ti at lower oxidation state in the surface region of all samples, as indicated by the absence of the shoulder peaks associated with  $\text{Ti}^{3+}$  at 456.8 eV and 462.5 eV for  $2p_{3/2}$  and  $2p_{1/2}$  core level of  $\text{Ti}^{3+}$ , respectively [39]. It is widely believed that  $\text{Ti}^{3+}$  is easily oxidized by a proper oxidant like  $\text{O}_2$  in air or dissolved oxygen in water, and thereby surface  $\text{Ti}^{3+}$  will be consumed rapidly [40]. TGA analysis also confirms the

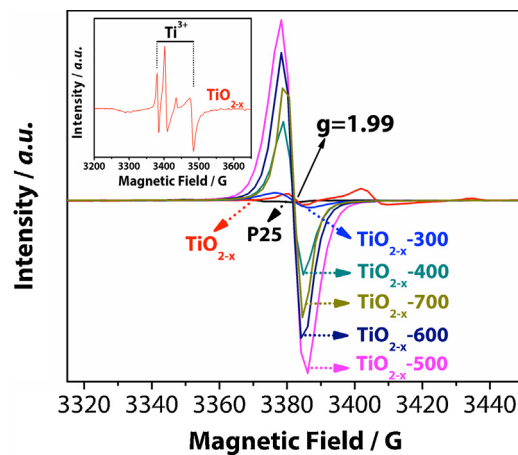


**Fig. 4.** EPR spectra of P25, as-prepared  $\text{TiO}_{2-x}$  and  $\text{TiO}_{2-x}-T$  samples at 110 K. (For interpretation of the references to color in the text, the reader is referred to the web version of this article.)

thermal stability of as-prepared samples which can retain their states up to 170 °C in air without obvious weight loss (c.f. Fig. S1). Given to that all of the samples exhibit excellent thermal and crystal stability in air at room temperature for 8 months without fading of colors, it can be certain that no  $\text{Ti}^{3+}$  species is located on surface in all samples.

The presence and quantity of bulk and subsurface  $\text{Ti}^{3+}$  in as-prepared samples was further studied by electron paramagnetic resonance (EPR). As illustrated in Fig. 4, the black line for commercial Degussa P25 shows a negligible paramagnetic signal peak under the present EPR measurement condition at 110 K. In general, the surface  $\text{Ti}^{3+}$  tends to adsorb  $\text{O}_2$ , which could be reduced to superoxide radical anions ( $\text{O}_2^-$ ) with an EPR signal feature at  $g = 2.02$  [41]. However, no such signal appears for all samples, further illustrating the absence of surface  $\text{Ti}^{3+}$ . As shown in the localized amplification inset of Fig. 4, the  $\text{TiO}_{2-x}$  sample exhibits a  $g$  value ranging from 1.93 to 1.99. This broad hallmark signal peak demonstrates that there are multiple paramagnetic species with different  $g$  values and hyperfine splittings in as-prepared  $\text{TiO}_{2-x}$  nanoparticles. The signals are attributed to electrons trapping to produce  $\text{Ti}^{3+}$  in bulk anatase. On the other hand, the EPR spectra of anatase  $\text{TiO}_{2-x}-T$  nanoparticles show intense axially symmetry signals centered on the  $g$  value of 1.99, which have been extensively reported for  $\text{Ti}^{3+}$  ions in anatase crystallite [28], indicating that the free electrons occupy interior Ti position thereby generating  $\text{Ti}^{3+}$  defects. Notably, the type of EPR characteristic signals between as-prepared  $\text{TiO}_{2-x}$  and  $\text{TiO}_{2-x}-T$  samples are significantly different, inferring that  $\text{Ti}^{3+}$  exists in different distribution states. It is obvious that the signal intensities of anatase  $\text{TiO}_{2-x}-T$  samples are stronger compared to  $\text{TiO}_{2-x}$ .

As depicted in Fig. 4, the  $\text{TiO}_{2-x}-T$  samples after annealing at different temperatures exhibit varied EPR signal intensities. In the initial stage, when the annealing temperature ( $T$ ) gradually increases from 300 °C to 400 °C and up to 500 °C, the signal peak intensity appears at  $g = 1.99$ , which can be related to the color change from light blue to intense dark black. By numerical double integration of the EPR spectra with an aqueous solution of  $\text{Cu}^{2+}$  as reference, the amount of  $\text{Ti}^{3+}$  centers for  $\text{TiO}_{2-x}-300$  sample is calculated to be  $0.7 \times 10^{19}$  spins/mol, equivalent to one  $\text{Ti}^{3+}$  out of every  $2.9 \times 10^4$   $\text{Ti}^{4+}$ . Whereas, the amount of  $\text{Ti}^{3+}$  centers for  $\text{TiO}_{2-x}-500$  sample is almost 10 times larger than  $\text{TiO}_{2-x}-300$ , namely, one  $\text{Ti}^{3+}$  in every  $2.9 \times 10^3$   $\text{Ti}^{4+}$ . This suggests that the concentration of bulk  $\text{Ti}^{3+}$  defect is greatly enhanced by the high temperature post-annealing treatment. As illustrated in Fig. 5, this temperature-dependent defect-management can be understood in the way that

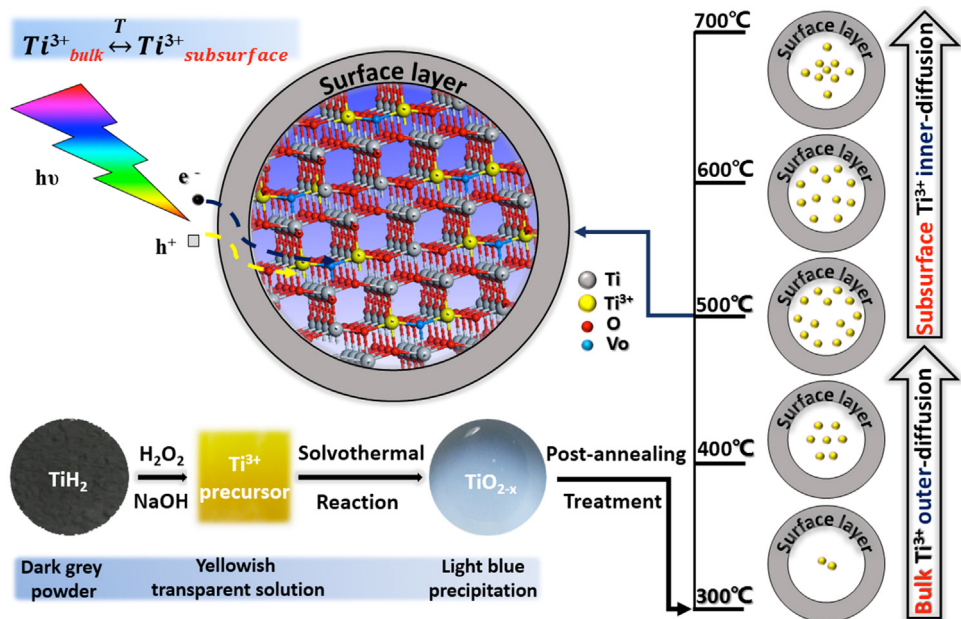


**Fig. 5.** Mechanism of  $\text{Ti}^{3+}$  distribution in as-prepared  $\text{TiO}_{2-x}$  and  $\text{TiO}_{2-x}-T$  samples.

higher temperature treatment promotes the entropy-driven diffusion of the bulk  $\text{Ti}^{3+}$  defects in the bulk of the as-prepared defective  $\text{TiO}_{2-x}$  nanocrystals ( $\text{TiO}_{2-x}$ ) toward the subsurface region of the crystals (out-diffusion). Thus, a well-controlled temperature can end up with such diffusion right near the surface layer. Indeed, the amount of  $\text{Ti}^{3+}$  does not always increase with increasing temperature. As temperature goes up to 600 °C and 700 °C, the resonance signal intensity decreases slowly because higher energy breaks the saturated state of  $\text{Ti}^{3+}$  subsurface/bulk distribution. Compared with  $\text{TiO}_{2-x}-500$  sample,  $\text{TiO}_{2-x}-600$ , with the much smaller number of  $\text{Ti}^{3+}$  centers as  $4.3 \times 10^{19}$  spins/mol were observed. For  $\text{TiO}_{2-x}-700$ , the number of  $\text{Ti}^{3+}$  centers is  $3.3 \times 10^{19}$  spins/mol, even lower than  $\text{TiO}_{2-x}-600$ . The further diffusion of  $\text{Ti}^{3+}$  defect is quite difficult due to the increase in the crystallinity and insufficient dynamic driving force supply (no surface adsorbed oxygen during post-annealing treatment process in an inert gas atmosphere). Meanwhile, the reverse process (inner-diffusion) will occur from the subsurface to the inner bulk. In order to verify this  $\text{Ti}^{3+}$  reversible-diffusion mechanism, the as-prepared  $\text{TiO}_{2-x}$  samples was post-annealed at 800 °C and 900 °C (Fig. S2) under the same condition with  $\text{TiO}_{2-x}-T$  samples. The color of  $\text{TiO}_{2-x}-800$  sample presents soft light blue and the  $\text{TiO}_{2-x}-900$  samples turns to white. The EPR signal peak of  $\text{TiO}_{2-x}-900$  disappears (Fig. S3), presumably due to that the  $\text{Ti}^{3+}$  defects as “color centers” are diluted at the beginning and vanished eventually.

### 3.3. Photocatalytic degradation activity and its mechanism analysis

The photoactivity of  $\text{TiO}_{2-x}-T$  is evaluated by the photodegradation of MB under visible light irradiation and the results are shown in Fig. 6a. For comparison, a blank experiment without the presence of catalyst and the experiment in the presence of commercial Degussa P25 were also performed; in both cases, the degree of MB concentration change is very limited. The concentration ratio ( $C/C_0$ ) of MB plotted against visible light irradiation time in the presence of the  $\text{Ti}^{3+}$  self-doped  $\text{TiO}_2$  catalysts shows the photocatalytic oxidation activity of respective samples. As expected, the  $\text{TiO}_{2-x}-T$  samples exhibit higher photodegradation activity compared with its counterpart,  $\text{TiO}_{2-x}$  sample. In particular, the  $\text{TiO}_{2-x}-500$  shows the highest catalytic activity, with 98.2% of the MB decomposed in

30 min. On the basis of the observed photocatalytic activities, the quantum efficiency (QE) for MB photodegradation by the prepared  $\text{TiO}_{2-x}-500$  catalyst was calculated using the following equation:  $\text{QE} = \text{Rr}/\text{Ra}$ , where  $\text{Rr}$  is the rate of change in the concentration of the reactant and  $\text{Ra}$  is the absorption rate of total photons impinging on the sample. The details of this calculation are described in the Supporting information (Fig. S4). The QE for MB photodegradation by  $\text{TiO}_{2-x}-500$  is 31%, which is the highest value among the  $\text{TiO}_{2-x}-T$  photocatalysts. To quantitatively compare the photocatalytic performances of  $\text{TiO}_{2-x}-T$  samples, the apparent rate constant for MB photodegradation ( $k$ ) was computed using the pseudo-first-order approximation, as shown in Fig. S5. Samples annealed at 300 and 400 °C, with rate constant  $k$  is  $0.0359 \text{ min}^{-1}$  and  $0.0552 \text{ min}^{-1}$ , respectively, show relatively lower photodegradation activity than  $\text{TiO}_{2-x}-500$  ( $k = 0.1303 \text{ min}^{-1}$ ). On the other hand,  $\text{TiO}_{2-x}-600$  ( $k = 0.0889 \text{ min}^{-1}$ ) and  $\text{TiO}_{2-x}-700$  ( $k = 0.0759 \text{ min}^{-1}$ ) also give relative lower photodegradation activity compared with  $\text{TiO}_{2-x}-500$ , but are still higher than that of  $\text{TiO}_{2-x}-400$ . Cycling stability tests (Fig. 6b) of  $\text{TiO}_{2-x}-500$  sample under the same condition shows nearly no deterioration in photocatalytic activity for the degradation of MB after 6 cycles.

Many factors could affect the activity of a photocatalyst, including particle size, specific surface area, crystallinity and so on. As derived by XRD, TEM and BET measurements, the particle size of  $\text{TiO}_{2-x}-T$  increases with treatment temperature while specific surface area decreases. Generally, increase in particle size or decrease in surface area would not be beneficial to a photocatalytic reaction. If this were the case in the present work, the photoactivity of  $\text{TiO}_{2-x}-T$  would decrease with treatment temperature. Indeed, as evaluated with the model reaction of MB degradation (Fig. 6a), the photoactivity of  $\text{TiO}_{2-x}-T$  follows the order:  $\text{TiO}_{2-x}-500 > \text{TiO}_{2-x}-600 > \text{TiO}_{2-x}-700 > \text{TiO}_{2-x}-400 > \text{TiO}_{2-x}-300$ . The activity order agrees well with the contents of  $\text{Ti}^{3+}$  in these samples as observed from quantitative EPR measurements (Fig. 4). This implies the importance of regulating the concentration and distribution of subsurface/bulk  $\text{Ti}^{3+}$  defects in  $\text{TiO}_2$ -based photocatalysts toward improved photoactivity.

In addition, the transient photocurrent response of the samples was examined with several on-off cycles using a typical three-electrode method under discontinuous irradiation to qualitatively probe the visible-light induced charge separation efficiency (see

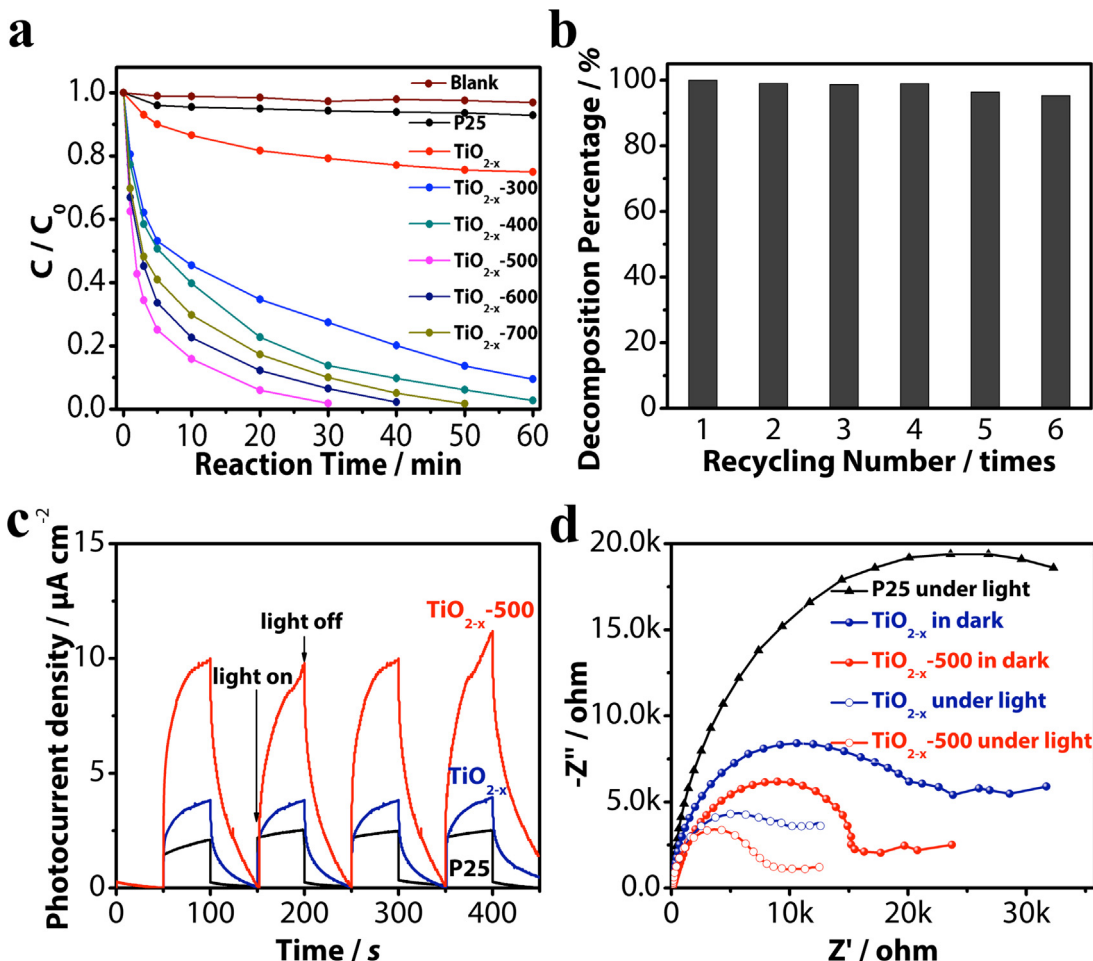


**Fig. 6.** (a) Photodegradation of methylene blue (MB) under visible light irradiation in the presence of various photocatalysts ( $[\text{MB}] = 20 \text{ ppm}$ , loading of catalyst is  $2 \text{ mg/L}$ ), and a blank experiment is provided as control. (b) Recycling test results for the  $\text{TiO}_{2-x}$ -500 sample. (c) Transient photocurrent response (TPC) performance of P25,  $\text{TiO}_{2-x}$  and  $\text{TiO}_{2-x}$ -500: amperometric transient photocurrent density vs time plots under illumination of visible light with  $\lambda \geq 420 \text{ nm}$  and 50 s light on/off cycles. (d) Electrochemical impedance spectra of Nyquist plots ( $Z'$  vs  $-Z''$ ) in the dark and under light.

Fig. 6c). Degussa P25 was used as a benchmark of photocatalyst in the visible-light region. The photocurrent values obtained were normalized by the  $I_{\text{ph,in}}/I_{\text{ph,st}}$  ratio, where  $I_{\text{ph,in}}$  and  $I_{\text{ph,st}}$  correspond to the initial and stationary photocurrents, respectively. An electrode with a high  $I_{\text{ph,in}}/I_{\text{ph,st}}$  ratio and  $I_{\text{ph}}$  suggests a low rate of recombination during photoreaction. The  $I_{\text{ph,in}}/I_{\text{ph,st}}$  of the  $\text{TiO}_{2-x}$  is 4.0, whereas that of the  $\text{TiO}_{2-x}$ -500 is 10.0, a 3.3-fold and 8.3-fold increase compared to that for Degussa P25 ( $I_{\text{ph,in}}/I_{\text{ph,st}} = 1.2$ ), respectively. In comparison, the photocurrent of P25 disappears immediately after cut off the illumination, while both  $\text{TiO}_{2-x}$  and  $\text{TiO}_{2-x}$ -500 samples exhibit a residual current. The relatively slower decay of the photocurrent of  $\text{TiO}_{2-x}$ -T is indicative to the trapped charge carriers with a prolonged lifetime, a necessary characteristic for good photocatalysts [42,43].

Electrochemical impedance spectra (EIS) measurement was conducted to investigate the interfacial electrical properties between electrodes and solutions. Since the diameters of the semicircles are equal to the charge-transfer resistance of a sample, semicircles in Nyquist plots reveal the information on the charge transfer process. Based on previous studies, the smaller size of the semicircle arc diameter implies a more effective separation of the photogenerated e-h pairs and/or a faster interfacial charge transfer to the electron donor-acceptor [44]. As depicted in Fig. 6d, the  $\text{TiO}_{2-x}$ -500 exhibits the smallest semicircular diameter compared to other  $\text{TiO}_{2-x}$  samples both in the dark and under visible-light illumination, illustrating enhanced electronic conductivity in

$\text{TiO}_{2-x}$ -500 nanoparticles. This also supports that the  $\text{TiO}_{2-x}$ -500 possesses the highest photocatalytic activity.

Furthermore, the pathway of MB degradation was analyzed with HPLC-MS measurements. The MS (ESI) spectrum (Fig. 7) obtained at 0 min of the reaction shows only a single strong peak at  $m/z = 283$  with retention time ( $t_R$ ) of 1.29 min (as shown in Table 2), corresponding to the methylene blue ion. After 15 min of reaction in the presence of  $\text{TiO}_{2-x}$ -500 catalyst, the intensity of the peak at  $m/z = 283$  is decreased to 41% compared to reactant at 0 min. A new peaks appearing at  $m/z = 300$ , suggesting that hydroxyl group is incorporated into the aromatic ring of MB [45].

The spectrum at 30 min shows no peak at  $m/z = 283$ , indicating that the MB dye is totally decomposed to smaller fragments in 30 min. The peak at  $m/z = 135$  ( $t_R = 1.03$ ) is attributed to benzothiazole and the intensity is almost equal at 15 min and 30 min, indicating benzothiazole is mainly formed in the first 15 min without further degradation. The peak at  $m/z = 124$  ( $t_R = 4.32$ ), 111 ( $t_R = 1.65$ ) and 97 ( $t_R = 1.53$ ) decrease at 30 min, suggesting benzenediol, 1,2-benzoquinone and muconic acid are consumed to form the smaller fragments like oxalic acid. The peak at  $m/z = 91$  ( $t_R = 1.39$ ) is due to oxalic acid, which confirms above statement. MS spectra for all intermediates generated in the MB degradation at  $\text{TiO}_{2-x}$ -500 are given in Fig. S6. According to the intermediates and final products detected, the degradation mechanism for MB is proposed as shown in Fig. 8.

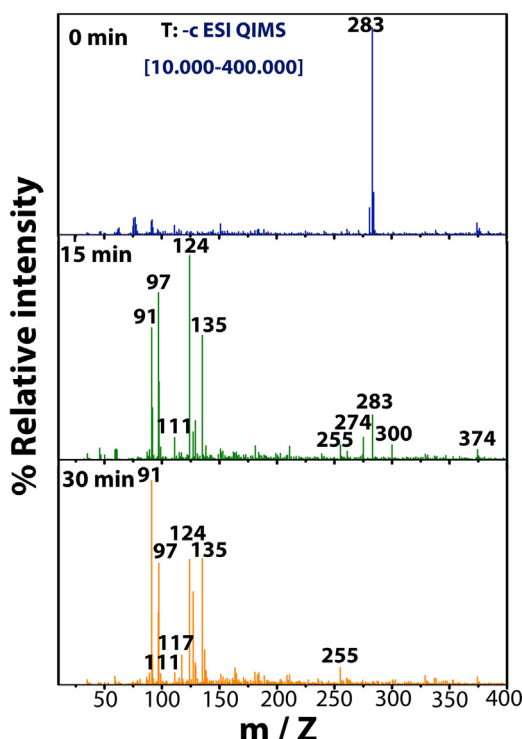


**Fig. 7.** Mass (ESI) spectra for monitoring the degradation products of MB by  $\text{TiO}_{2-x}$ -500 sample in 30 min.

During the dissolution of MB, most  $\text{Cl}^-$  may be ionized in the initial stage. N– $\text{CH}_3$  band is first broken and the – $\text{CH}_3$  is oxidized to HCHO or  $\text{HCOOH}$  [46]. C–S and C–N bands are broken in the following oxidation of the remaining structure. These organic

**Table 2**  
The intermediate and final products resulting from the  $\text{TiO}_{2-x}$ -500 degradation of MB in 30 min detectives by HPLC–MS.

Retention time ( $t_R$ )/min	Intermediate	$m/z$ value
4.32		124
1.65		111
1.03		135
1.53		97
1.4		117
1.39		91

intermediates in solution were further oxidized until finally transformed into  $\text{CO}_2$ ,  $\text{H}_2\text{O}$ ,  $\text{Cl}^-$ ,  $\text{SO}_4^{2-}$  and  $\text{NO}_3^-$ . The total organic carbon (TOC) tests show that the mineralization rate of MB at  $\text{TiO}_{2-x}$ -500 is apparently higher than that at P25 under the irradiation of visible light, as depicted in Fig. S7. The total organic carbon removed at  $\text{TiO}_{2-x}$ -500 sample is 50.3% within 30 min. This result further supports the proposed degradation mechanism for MB.

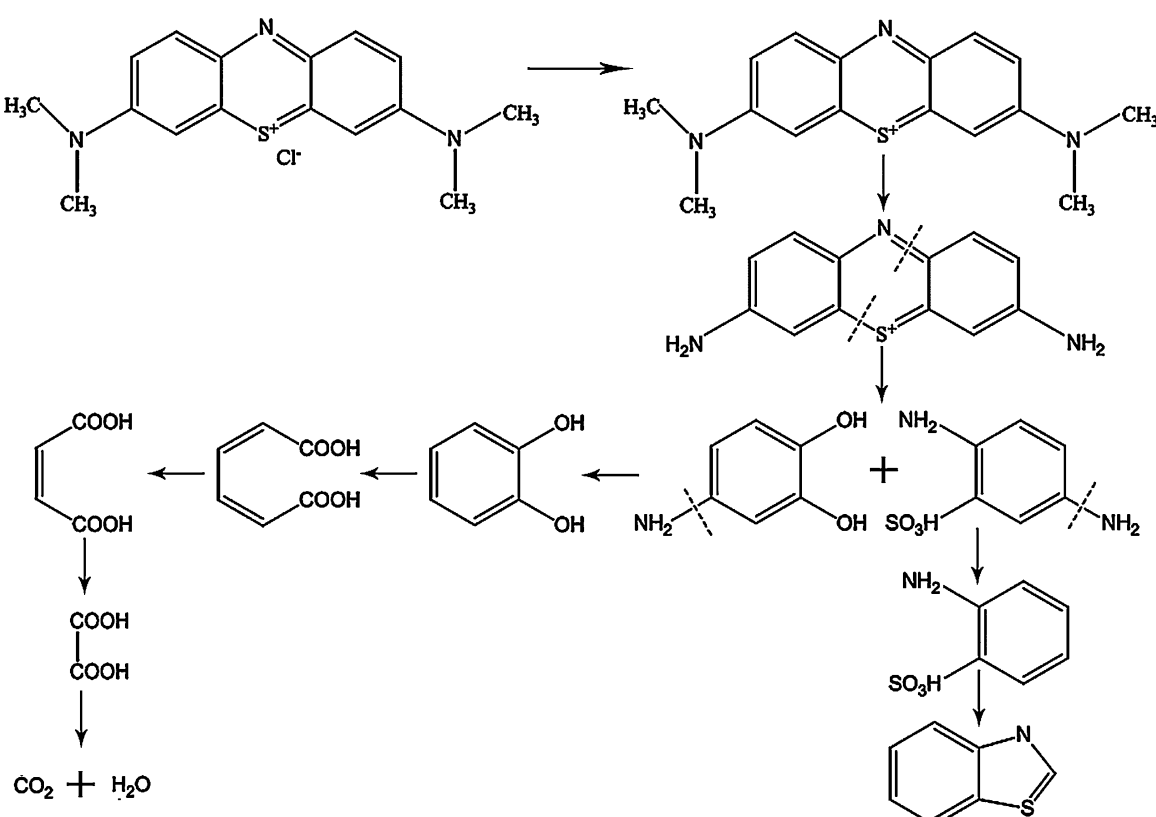


**Fig. 8.** Proposed degradation pathway of MB by  $\text{TiO}_{2-x}$ -500 sample under visible-light irradiation.

#### 4. Conclusions

In summary, this work demonstrates that the oxidation-based solvothermal synthesis of Ti<sup>3+</sup> self-doped anatase TiO<sub>2</sub> is an effective strategy to prepare uniform Ti<sup>3+</sup> self-doped anatase TiO<sub>2</sub> nanocrystals. Through a simple and innovative post-annealing treatment, the location of the Ti<sup>3+</sup> defects can be effectively controlled predominately in the subsurface/bulk regions of the anatase nanocrystals, while retaining the highest Ti<sup>3+</sup> concentration, leading to the remarkably enhanced photocatalytic activity and stability. The present work underlines the importance of proper distribution of subsurface/bulk Ti<sup>3+</sup> defects and give impetus to the development of the “defect engineering” of TiO<sub>2</sub> nanocrystals toward high visible light-driven photoactivity.

#### Acknowledgments

Financial support by the National Nature Science Foundation of China (Grant Nos. 21173261, 21303258), the Xinjiang International Science & Technology Cooperation Program, China (20146006), the “One Hundred Talents Project Foundation Program” of Chinese Academy of Sciences, the “Cross-Cooperation Program for Creative Research Teams” of Chinese Academy of Sciences, the Western Light Program of Chinese Academy of Sciences (XBBS201211), the “Western Action Plan” (KGZD-EW-502), and the Xinjiang Program of Cultivation of Young Innovative Technical Talents (2013731019) is gratefully acknowledged. TX also acknowledges the support from the U.S. National Science Foundation (CBET-1150617).

#### Appendix A. Supplementary data

Supplementary data associated with this article can be found, in the online version, at <http://dx.doi.org/10.1016/j.apcatb.2015.04.016>.

#### References

- [1] A. Fujishima, X.T. Zhang, D.A. Tryk, *Surf. Sci. Rep.* 63 (2008) 515–582.
- [2] M.R. Hoffmann, S.T. Martin, W. Choi, D.W. Bahnemann, *Chem. Rev.* 95 (1995) 69–96.
- [3] F. Zuo, L. Wang, T. Wu, Z.Y. Zhang, D. Borchardt, P.Y. Feng, *J. Am. Chem. Soc.* 132 (2010) 11856–11857.
- [4] X. Chen, L. Liu, P.Y. Yu, S.S. Mao, *Science* 331 (2011) 746–750.
- [5] X. Liu, F. Huang, X. Mou, Y. Wang, F. Xu, *Adv. Mater.* 22 (2010) E150–E155.
- [6] P. Periyat, D.E. McCormack, S.J. Hinder, S.C. Pillai, *J. Phys. Chem. C* 113 (2009) 3246–3253.
- [7] R. Asahi, T. Morikawa, T. Ohwaki, K. Aoki, Y. Taga, *Science* 293 (2001) 269–271.
- [8] S. Liu, N. Zhang, Z.-R. Tang, Y.-J. Xu, *ACS Appl. Mater. Interfaces* 4 (2012) 6378–6385.
- [9] K. Su, Z. Ai, L. Zhang, *J. Phys. Chem. C* 116 (2012) 17118–17123.
- [10] J.P. Wang, B.B. Huang, Z.Y. Wang, P. Wang, H.F. Cheng, Z.K. Zheng, X.Y. Qin, X.Y. Zhang, Y. Dai, M.-H. Whangbo, *J. Mater. Chem.* 21 (2011) 4562–4567.
- [11] D. Li, Z. Chen, Y. Chen, W. Li, H. Huang, Y. He, X. Fu, *Environ. Sci. Technol.* 42 (2008) 2130–2135.
- [12] R. Mukherjee, A.V. Thomas, D. Datta, E. Singh, J.W. Li, O. Eksik, V.B. Shenoy, N. Koratkar, *Nat. Commun.* 5 (2014) 3710–3719.
- [13] V. Etacheri, M.K. Seery, S.J. Hinder, S.C. Pillai, *Adv. Funct. Mater.* 21 (2011) 3744–3752.
- [14] F. Zuo, K. Bozjilov, R.J. Dillon, L. Wang, P. Smith, X. Zhao, C. Bardeen, P. Feng, *Angew. Chem. Int. Ed. English* 51 (2012) 6223–6226.
- [15] K.K. Adepalii, M. Kelsch, R. Merkle, J. Maier, *Adv. Funct. Mater.* 23 (2013) 1798–1806.
- [16] X.Y. Pan, M.Q. Yang, X.Z. Fu, N. Zhang, Y.J. Xu, *Nanoscale* 5 (2013) 3601–3614.
- [17] S.M. Prokes, J.L. Gole, X.B. Chen, C. Burda, W.E. Carlos, *Adv. Funct. Mater.* 15 (2005) 161–167.
- [18] I. Nakamura, N. Negishi, S. Kutsuna, T. Ihara, S. Sugihara, K. Takeuchi, *J. Mol. Catal. A Chem.* 161 (2000) 205–212.
- [19] H. Liu, H.T. Ma, X.Z. Li, W.Z. Li, M. Wu, X.H. Bao, *Chemosphere* 50 (2003) 39–46.
- [20] J.-Y. Shin, J.H. Joo, D. Samuelis, J. Maier, *Chem. Mater.* 24 (2012) 543–551.
- [21] A. Naldoni, M. Allieta, S. Santangelo, M. Marelli, F. Fabbri, S. Cappelli, C.L. Bianchi, R. Psaro, V.D. Santo, *J. Am. Chem. Soc.* 134 (2012) 7600–7603.
- [22] G. Wang, H. Wang, Y. Ling, Y. Tang, X. Yang, R.C. Fitzmorris, C. Wang, J.Z. Zhang, Y. Li, *Nano Lett.* 11 (2011) 3026–3033.
- [23] I. Nakamura, S. Sugihara, K. Takeuchi, *Chem. Lett.* 29 (2000) 1276–1277.
- [24] Z.K. Zhang, M.L. Bai, D.Z. Guo, S.M. Hou, G.M. Zhang, *Chem. Commun.* 47 (2011) 8439–8441.
- [25] M. Xing, J. Zhang, F. Chen, B. Tian, *Chem. Commun.* 47 (2011) 4947–4949.
- [26] Z. Pei, L. Ding, H. Lin, S. Weng, Z. Zheng, Y. Hou, P. Liu, *J. Mater. Chem. A* 1 (2013) 10099–10102.
- [27] M. Liu, X. Qiu, M. Miyachi, K. Hashimoto, *Chem. Mater.* 23 (2011) 5282–5286.
- [28] J.G. Wang, P. Zhang, X. Li, J. Zhu, H.X. Li, *Appl. Catal. B: Environ.* 134–135 (2013) 198–204.
- [29] L.R. Grabstanowicz, S. Gao, T. Li, R.M. Rickard, T. Rajh, D.-J. Liu, T. Xu, *Inorg. Chem.* 52 (2013) 3884–3890.
- [30] X.M. Yu, B. Kim, Y.K. Kim, *ACS Catal.* 3 (2013) 2479–2486.
- [31] D.Y. Qi, L.J. Lu, Z.H. Xi, L.Z. Wang, J.L. Zhang, *Appl. Catal. B: Environ.* 160–161 (2014) 621–628.
- [32] V. Likodimos, T. Stergiopoulos, P. Falaras, J. Kunze, P. Schmuki, *J. Phys. Chem. C* 112 (2008) 12687–12696.
- [33] G. Liu, H.G. Yang, X.W. Wang, L.N. Cheng, H.F. Lu, L.Z. Wang, G.Q. Lu, H.M. Cheng, *J. Phys. Chem. C* 113 (2009) 21784–21788.
- [34] Q. Zhu, Y. Peng, L. Lin, C.M. Fan, G.Q. Gao, R.X. Wang, A.W. Xu, *J. Mater. Chem. A* 2 (2014) 4429–4437.
- [35] S.K. Gupta, R. Desai, P.K. Jha, S. Sahoo, D.J. Kirinc, *Raman Spectrosc.* 41 (2010) 350–355.
- [36] Z. Wang, C.Y. Yang, T.Q. Lin, H. Yin, P. Chen, D.Y. Wan, F.F. Xu, F.Q. Huang, J.H. Lin, X.M. Xie, M.H. Jiang, *Energy Environ. Sci.* 6 (2013) 3007–3014.
- [37] H. Zhang, Y. Zhao, S. Chen, B. Yu, J. Xu, H. Xu, L. Hao, Z. Liu, *J. Mater. Chem. A* 1 (2013) 6138–6144.
- [38] S. Hoang, S.P. Berglund, N.T. Hahn, A.J. Bard, C.B. Mullins, *J. Am. Chem. Soc.* 134 (2012) 3659–3662.
- [39] Z.H. Zhang, X.L. Yang, M.N. Hedhili, E. Ahmed, L. Shi, P. Wang, *ACS Appl. Mater. Interfaces* 6 (2014) 691–696.
- [40] A. Teleki, S.E. Pratsinis, *Phys. Chem. Chem. Phys.* 11 (2009) 3742–3747.
- [41] M. Anpo, M. Che, B. Fubini, E. Garrone, E. Giamello, M. Paganini, *Top. Catal.* 8 (1999) 189–198.
- [42] J. Zhuang, S. Weng, W. Dai, P. Liu, Q. Liu, *J. Phys. Chem. C* 116 (2012) 25354–25361.
- [43] T.L. Thompson, J.T. Yates Jr., *Chem. Rev.* 106 (2006) 4428–4453.
- [44] X. Cheng, W. Leng, D. Liu, Y. Xu, J. Zhang, C. Cao, *J. Phys. Chem. C* 112 (2008) 8725–8734.
- [45] T. Sriskandakumar, N. Opembe, C.-H. Chen, A. Morey, C. King'ondu, S.L. Suib, *J. Phys. Chem. A* 113 (2009) 1523–1530.
- [46] Q. Wang, S. Tian, P. Ning, *Ind. Eng. Chem. Res.* 53 (2014) 643–649.